Supporting Information

Boosting Photothermal Conversion through Array Aggregation of Metalloporphyrins in Bismuth-based Coordination Frameworks

Liang He,[a] Jing He,[a] Er-Xia Chen,[a,c,*] and Qipu Lin[a,b,d,*]

[a] Key Laboratory of Structural Chemistry, Fujian Institute of Research on the Structure of

Matter, Chinese Academy of Sciences, Fuzhou, Fujian 350002, China

[b] University of Chinese Academy of Sciences, Beijing 100049, China

[c] Fujian Science & Technology Innovation Laboratory for Optoelectronic Information of China,

Fuzhou, Fujian 350108 China

[d] State Key Laboratory of Photocatalysis on Energy and Environment, Fuzhou University,

Fuzhou, 350116, China

Corresponding author E-mail: exchen@fjirsm.ac.cn; linqipu@fjirsm.ac.cn

Table of Contents

S1. Experimental Section

S1.1 Materials and General Methods

Chemicals: All chemical reagents and solvents were obtained from commercial supplies and used without further purification.

Powder X-ray diffraction (PXRD) was carried out with a Rigaku Dmax 2500 X-ray diffractometer with a Cu sealed tube (λ = 1.54178 Å); while variable temperature PXRD was collected on a Rigaku, Ultima-IV Desktop X-ray Diffractometer.

Elemental analysis (EA) was conducted on a Vario EL-Cube.

Fourier-transform infrared (FT-IR) spectroscopy was performed in the range 4000~400 cm^{-1} using KBr pellets on a Nicolet Magna 750 FT-IR spectrometer.

Thermogravimetric analysis (TGA) was executed on a Netzsch STA449C thermal analyzer at a temperature range of 25 to 800 °C under N_2 atmosphere with the heating rate of 10 °C min^{-1}.

Field emission scanning electron microscope (FE-SEM) images were obtained with a JSM6700-F microscope.

Ultraviolet-visible diffuse reflectance spectroscopy (UV-Vis DRS) was implemented on a Perkin Elmer Lambda950 UV-Vis. spectrophotometer from 250 to 800 nm using barium sulfate ($BaSO_4$) as a standard with 100% reflectance.

N_2/CO_2 sorption measurements were taken using a Micrometritics ASAP 2020 system.

S1.2. Synthetic Procedures

(1) Synthesis of NiTCPP and CoTCPP

NiTCPP and CoTCPP were synthesized following the procedures outlined in the references.[1]

(2) Synthesis of TCPP-Bi

TCPP-Bi were synthesized following the procedures outlined in the references.[2]

(3) Synthesis of nanoplates CoTCPP-Bi

A mixture of $Bi(NO_3)_3(H_2O)_5$ (20 mg), $Co(NO_3)_2(H_2O)_6$ (10 mg), tetrakis(4-carboxylphenyl)porphyrin (TCPP, 10 mg), *N,N*-dimethylformamide (DMF, 3 mL) and EtOH (0.5 mL) was sealed in a 23-mL vial and heated at 100 °C for 12 h. Upon cooling to room temperature, dark-brown crystals were obtained with a yield of 65% based on TCPP. Anal. Calcd (%): C 55.25, H 2.30, N 5.44, Co 5.70, Bi 20%; found: C 53.48, H 2.87, N 5.44, Co 4.76, Bi 14.42%.

(4) Synthesis of nanoplates NiTCPP-Bi

A mixture of $Bi(NO_3)_3(H_2O)_5$ (20 mg), $Ni(NO_3)_2(H_2O)_6$ (10 mg), tetrakis(4-carboxylphenyl)porphyrin (TCPP, 10 mg), *N,N*-dimethylformamide (DMF, 3 mL) and EtOH (0.5 mL) was sealed in a 23-mL vial and heated at 100 °C for 12 h. Upon cooling to room temperature, dark-brown crystals were obtained with a yield of 47% based on TCPP. Anal. Calcd (%): C 56.02, H 2.33, N 5.446, Ni 5.64, Bi 20.33%; found: C 52.53, H 2.79, N 5.38, Ni 4.06, Bi 16.86 %.

S2. Results and Discussion

S2.1. Crystallographic Data

(1) Crystallography

Single crystals of CoTCPP-Bi and NiTCPP-Bi were meticulously chosen under an optical microscope and affixed to a thin glass fiber. Single crystal XRD data were obtained using a ROD, Synergy Custom system, HyPix diffractometer equipped with micro-focus metaljet GaKα (λ = 1.3405 Å) radiation at a temperature of 100K. Data integration and reduction were processed with the CrysAlisPro program package from Rigaku Oxford Diffraction software. A multi-scan absorption correction was applied to the collected reflections. The structure was determined using the SHELXT program package, and refined on F^2 by a full-matrix least-squares technique using the SHELXL program package. All non-hydrogen atoms were refined anisotropically, while hydrogen positions were fixed at their calculated positions and refined isotropically.

Table S1. Crystallographic data of the titled compound

Compounds	CoTCPP-Bi	NiTCPP-Bi
Empirical formula	$C_{96}H_{48}Bi_2Co_2N_8O_{16}$	$C_{96}H_{48}Bi_2Ni_2N_8O_{16}$
Formula weight	2058.86	2056.42
Temperature/K	100	100
Crystal system	orthorhombic	orthorhombic
Space group	$P2_12_12$	$P2_12_12$
a/Å	41.3588(5)	41.7558(5)
b/Å	24.2856(3)	24.3040(3)
c/Å	9.2134(2)	9.26890(10)
α/°	90	90
β/°	90	90
γ/°	90	90
Volume/Å^3	9254.2(3)	9406.39(19)
Z	4	4
ρ_{calc}/g cm^{-3}	1.478	1.452
μ/mm^{-1}	7.185	7.316
$F(000)$	3924.0	3928.0
Radiation	GaKα (λ = 1.34050)	GaKα (λ = 1.34050)
2θ range for data collection/°	3.048 to 55.046	3.658 to 112.244
Reflections collected	33960	34582
Independent reflections	14549 [R_{int} = 0.0363, R_{sigma} = 0.0485]	17129 [R_{int} = 0.0722, R_{sigma} = 0.0784]
Goodness-of-fit on F^2	1.048	1.073
Final R indexes [$I>=2\sigma(I)$]	[a]R_1 = 0.0696, [b]wR_2 = 0.1679	[a]R_1 = 0.0707, [b]wR_2 = 0.1856
Final R indexes [all data]	[a]R_1 = 0.0739, [b]wR_2 = 0.1705	[a]R_1 = 0.0814, [b]wR_2 = 0.1920
CCDC No.	2323214	2356520

[a] $R_1 = \sum||\boldsymbol{F}_o| - |\boldsymbol{F}_c||/\sum|\boldsymbol{F}_o|$; [b] $wR_2 = [\sum w(\boldsymbol{F}_o{}^2 - \boldsymbol{F}_c{}^2)^2/\sum w(\boldsymbol{F}_o{}^2)^2]^{1/2}$.

(2) Additional Structural Figures
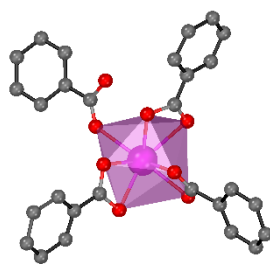
Figure S1. Four-connection secondary building unit [Bi(COO)$_4$].

Co$\cdots$C 3.047 Å   Co$\cdots$C 3.126 Å
Ni$\cdots$C 3.530 Å   Ni$\cdots$C 3.482 Å

Co$\cdots$C 3.238 Å   Co$\cdots$C 3.282 Å
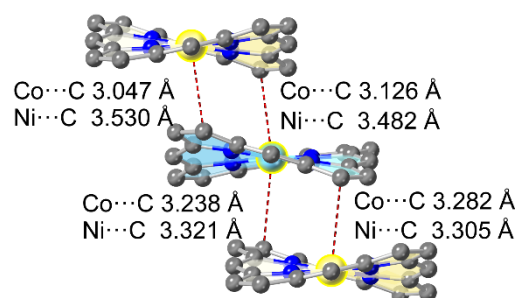Ni$\cdots$C 3.321 Å   Ni$\cdots$C 3.305 Å

Figure S2. Side view of the Co-C or Ni-C distances between neighbouring porphyrin macrocycles.
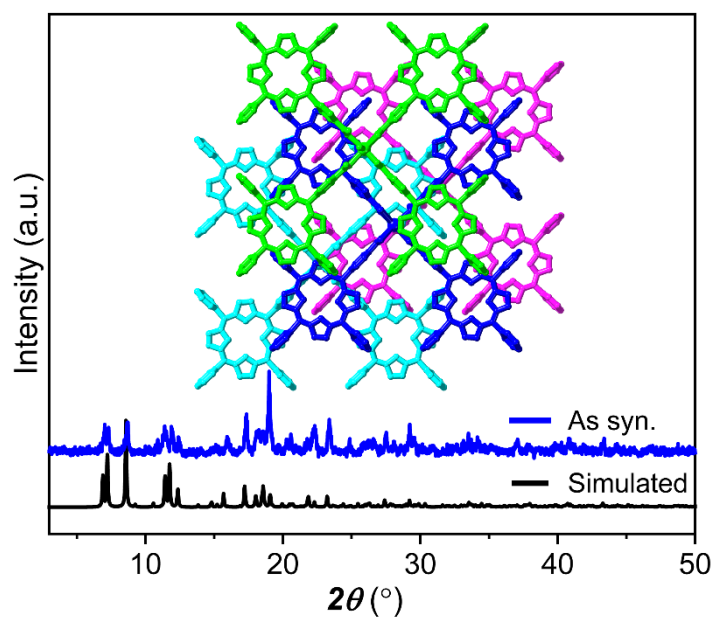
Figure S3. PXRD patterns of TCPP-Bi (the insert shows the structure of TCPP-Bi views along the c-axis of the stacking mode of 2D layers).

S2.2. Metal Content Analysis
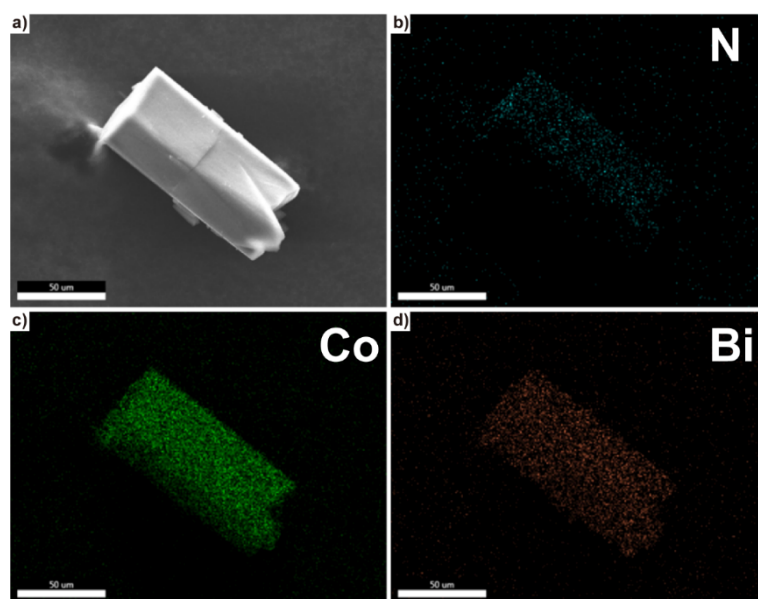
Figure S4. Elemental mapping images of CoTCPP-Bi.
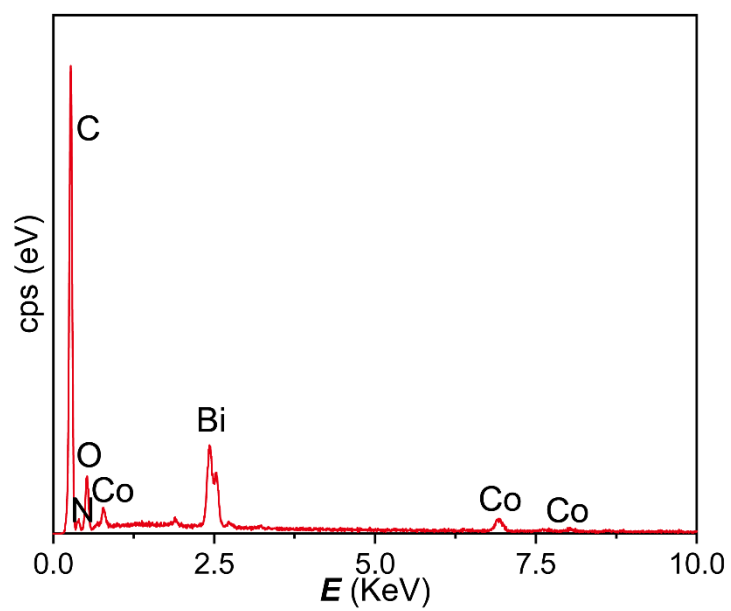
Figure S5. EDX spectrum of CoTCPP-Bi, revealing the existence of Co^{2+} and Bi^{3+} in the sample.
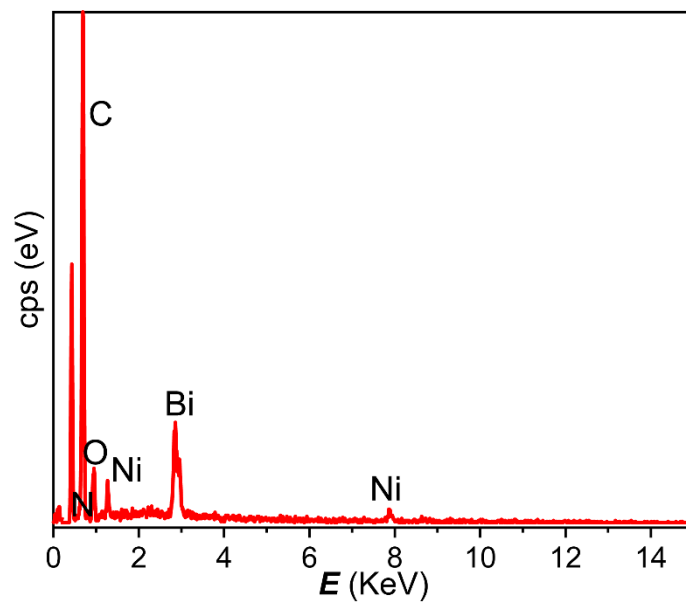
Figure S6. EDX spectrum of NiTCPP-Bi, revealing the existence of Ni^{2+} and Bi^{3+} in the sample.

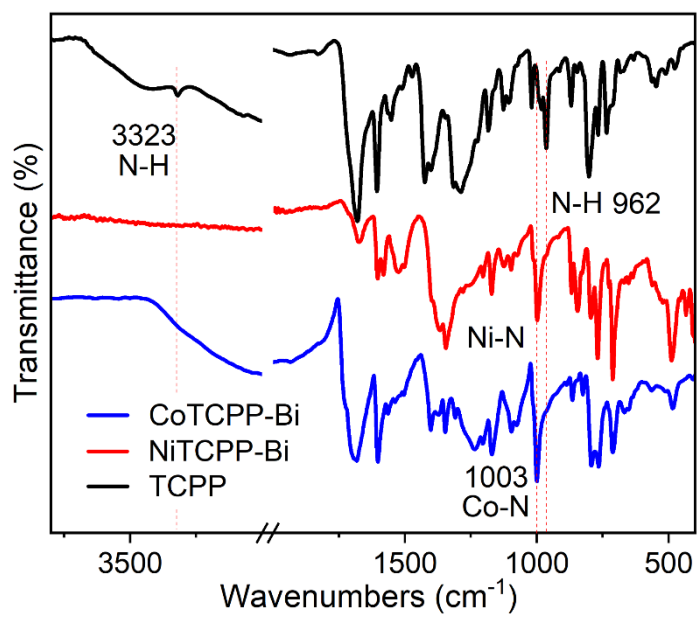**S2.3. Fourier-Transform Infrared (FT-IR) Spectroscopy**

Figure S7. FT-IR spectra of TCPP , NiTCPP-Bi, and CoTCPP-Bi.
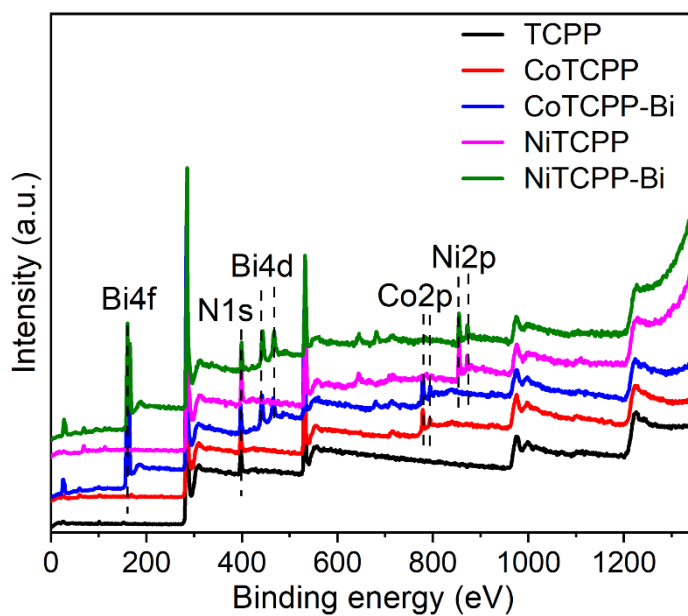
S2.4. X-ray Photoelectron Spectroscopy (XPS)

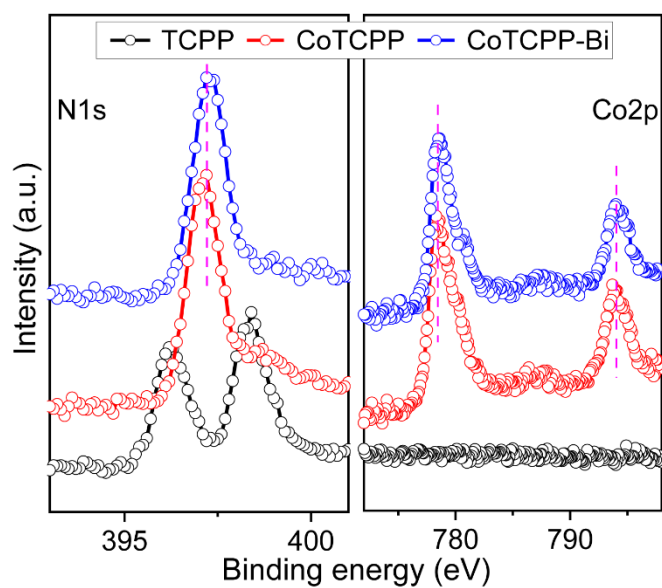**Figure S8.** XPS survey spectra of TCPP, CoTCPP, CoTCPP-Bi, NiTCPP, and NiTCPP-Bi, respectively.

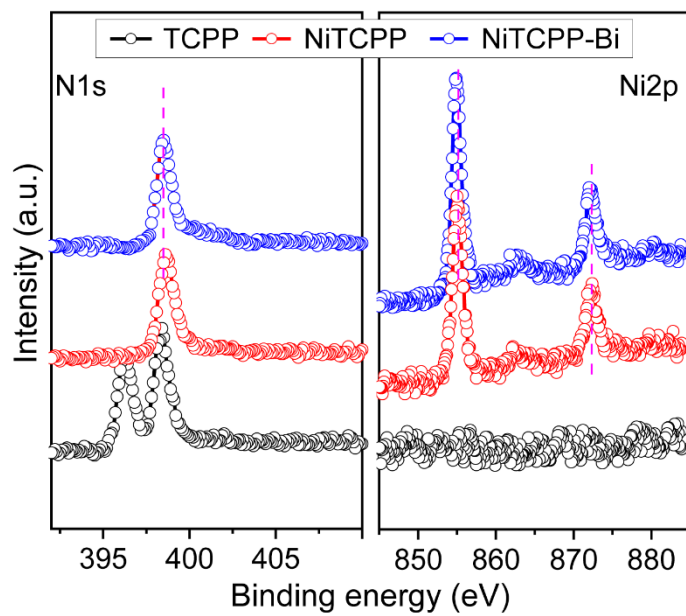**Figure S9.** XPS N1s spectra of TCPP, CoTCPP and CoTCPP-Bi, respectively.

Figure S10. XPS N1s spectra of TCPP, NiTCPP and NiTCPP-Bi, respectively.

S2.5. Theoretical Calculations

The geometry of these molecules were optimized using the density of functional theory (DFT) with the PBE0 functional[3] and def2SVP basis set.[4] The DFT-D3 dispersion correction method was incorporated in the calculations. All calculations were performed using the ORCA 5.0.2 program.[5] The electron spin density, defined as the difference between the α electron density and the β electron density, was computed using the Multiwfn program.[6] Visualization of the frontier molecular orbitals and electron spin density was achieved using the VESTA program.
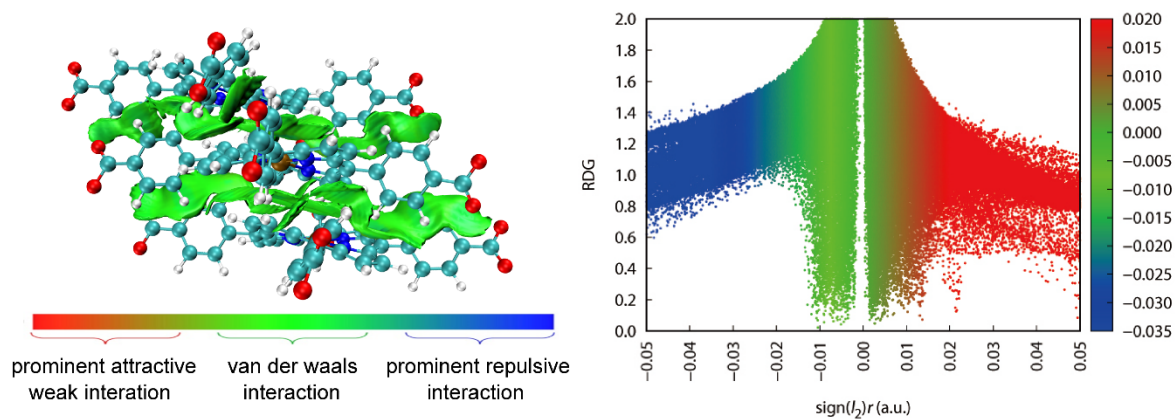

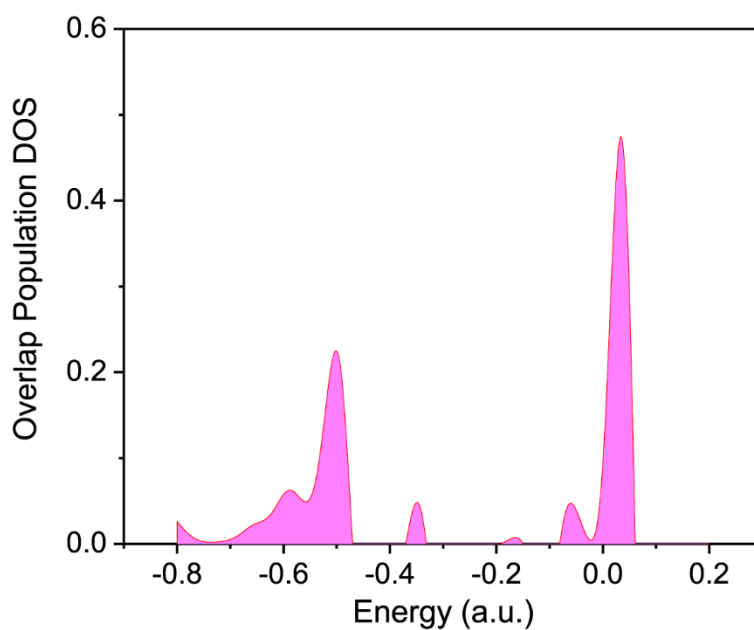**Figure S11.** Interlayer noncovalent interaction isosurfaces for CoTCPP-Bi.

Figure S12. Overlap in the density of states between adjacent layers in the bonding region (viz. the value is positive) for CoTCPP-Bi.
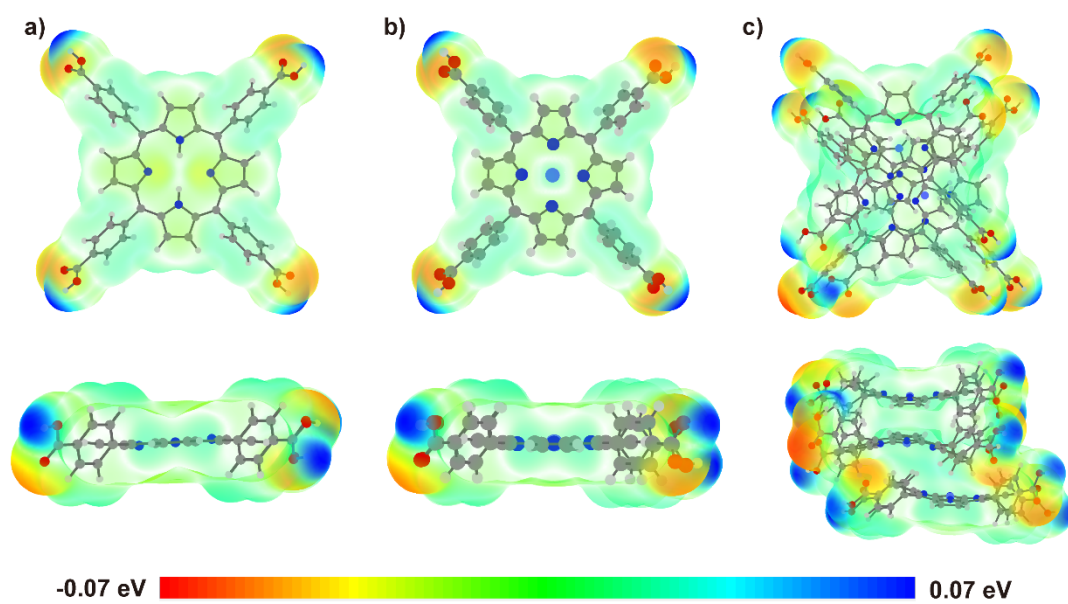
-0.07 eV **0.07 eV**

Figure S13. The electrostatic potential analysis of (a) TCPP, (b) CoTCPP, and (c) CoTCPP-Bi, respectively.

S2.6. Gas-Sorption Measurements

The measurement temperature was controlled by a liquid-nitrogen bath (77 K) and a dry ice-acetone bath (195 K). Prior to the sorption experiments, the as-synthesized samples underwent washing with DMF followed by immersion in acetone for 3 days. During this period, the solvent was decanted and freshly replenished three times. Subsequently, the samples were subjected to high vacuum treatment for 6 h at 393 K to remove residual solvents.
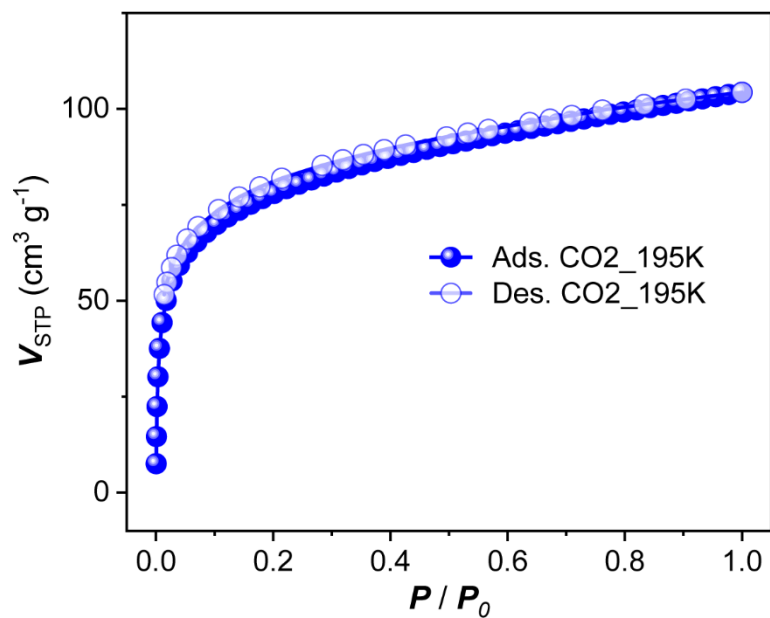

Figure S14. CO_2 adsorption-desorption isotherms recorded at 195 K for CoTCPP-Bi.

S2.7. Stability Analysis
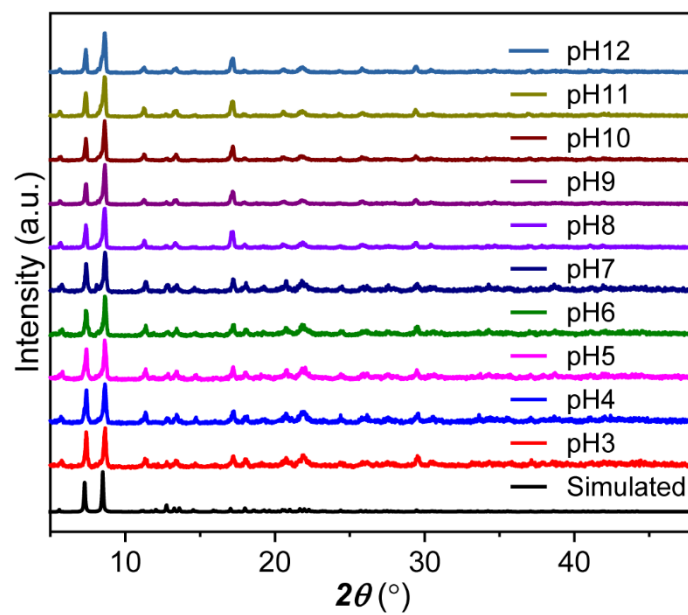
(a) Chemical Stability Analysis

Figure S15. PXRD patterns of CoTCPP-Bi after soaking in aqueous solutions spanning the pH range of 3~12 for 12h.
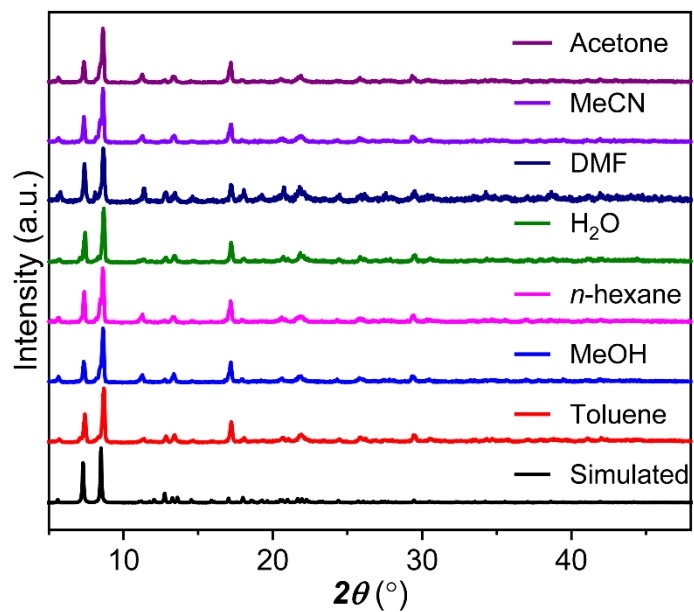
Figure S16. PXRD patterns of CoTCPP-Bi treated in different organic solvents for 12h.
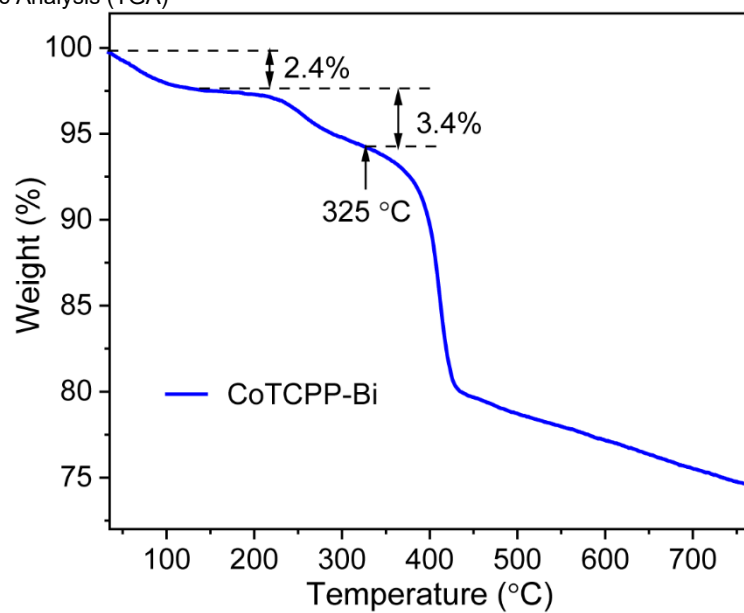
(b) Thermal Gravimetric Analysis (TGA)

Figure S17. TGA curve of CoTCPP-Bi under N_2 atmosphere.
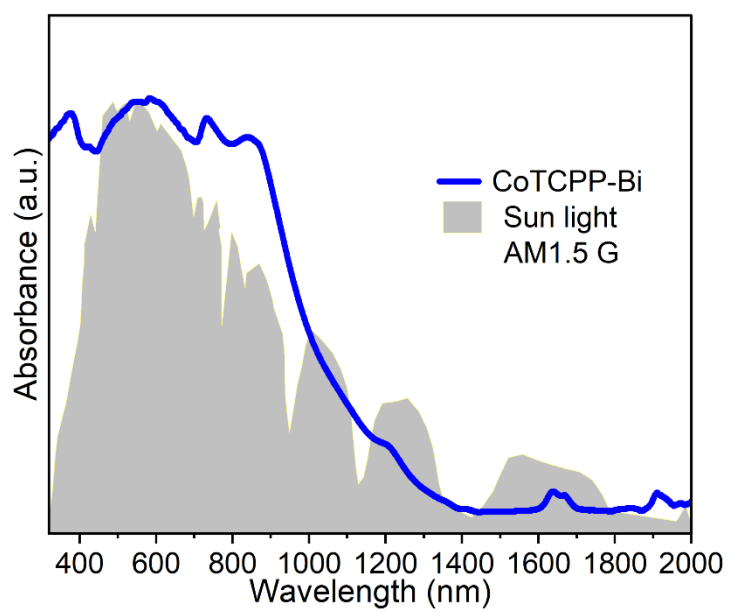
S2.8. UV-Vis-NIR absorption spectra

Figure S18. UV-Vis-NIR absorption spectra of powder samples of CoTCPP-Bi, and the solar spectral irradiance (AM 1.5 G).

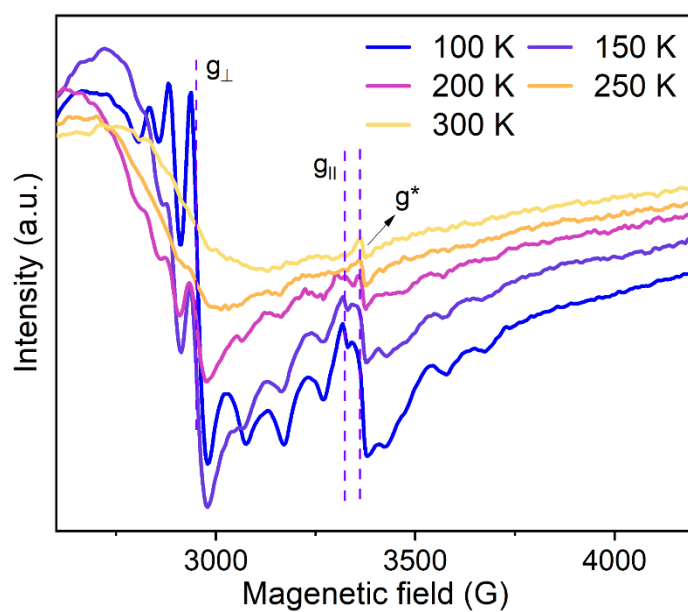**S2.9. Electron Paramagnetic Resonance (EPR) spectroscopy**

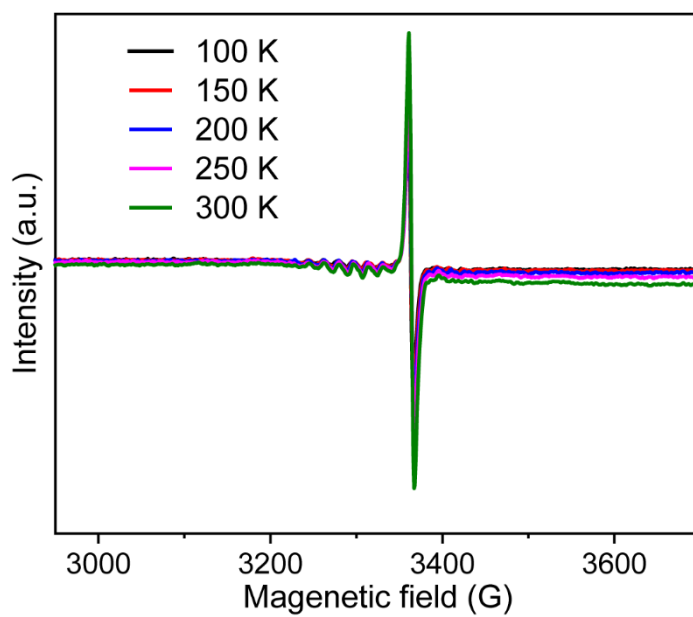**Figure S19.** Temperature-dependent EPR spectra of CoTCPP-Bi.

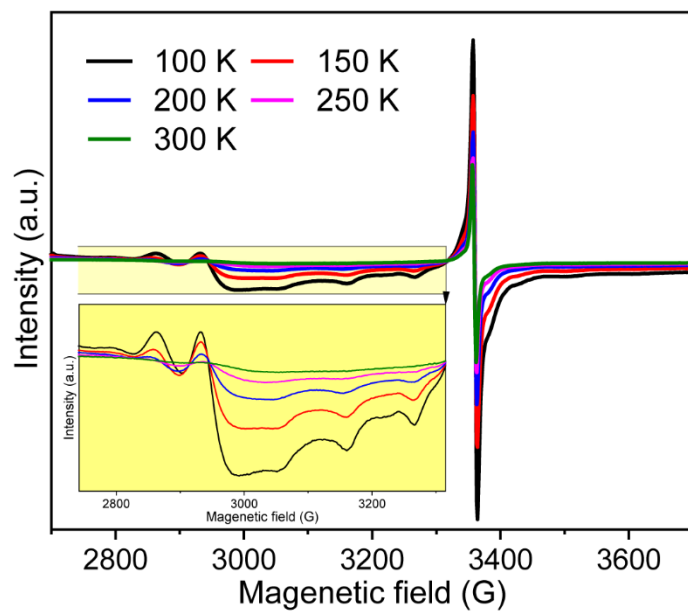**Figure S20.** Temperature-dependent EPR spectra of TCPP.

Figure S21. Temperature-dependent EPR spectra of CoTCPP.

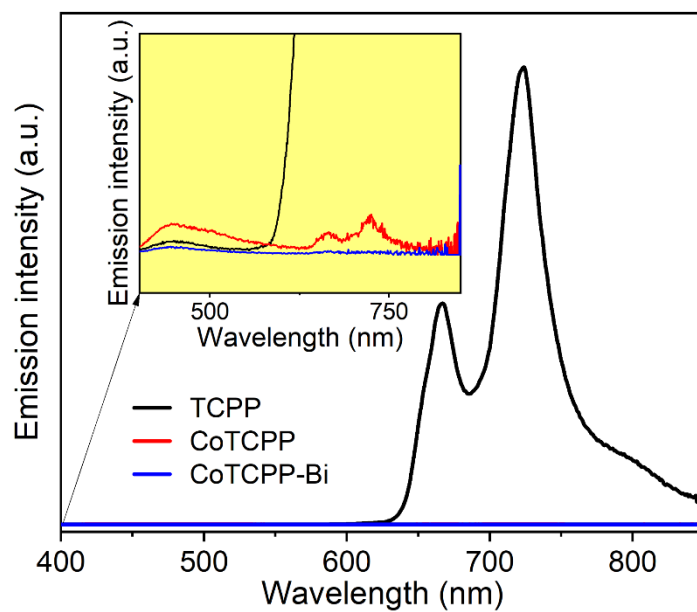## S2.10. Photoluminescence (PL) Spectroscopy

Figure S22. PL emission spectra of TCPP, CoTCPP and CoTCPP-Bi powders, respectively.

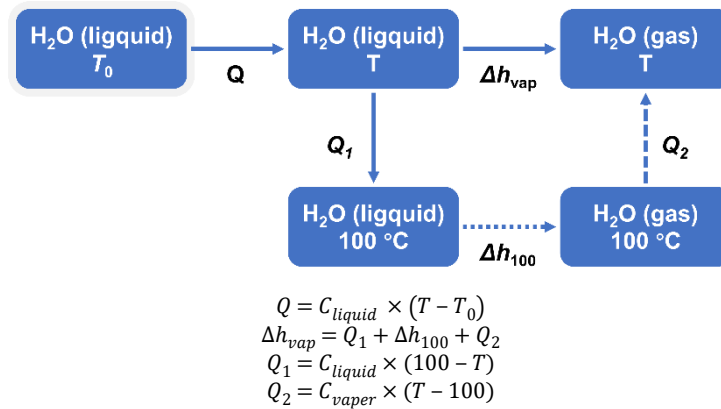## S2.11. Photothermal Conversion and Solar-Driven Water Evaporation.

An infrared (IR) thermal camera was utilized to record temperature data during the photothermal experiments. Prior to the commencement of the tests, the camera's temperature readings were calibrated to ensure precision and accuracy.

An 808 nm laser, equipped with a collimator and featuring adjustable power settings, in combination with a xenon lamp that provides adjustable power and is equipped with an AM1.5G filter, were utilized as the light sources for the study.

The efficiency (η) of solar energy conversion in photothermal-assisted water evaporation was calculated as the following formula.

$$\mu = \frac{\dot{m} h_{LV}}{C_{opt} P_0}$$

Where $\dot{m}$ refers to the mass flux of water, h_{LV} represents the total liquid-vapor phase transition enthalpy [i.e., sensible heat and vaporization enthalpy ($h_{LV} = Q + \Delta h_{vap}$)], and Q is the energy used to transform the system from the initial temperature T_0 to the final temperature T, Δh_{vap} denotes the latent heat of vaporization of water, P_0 refers to the nominal solar radiation value of 1 kW m^{-2}, and C_{opt} represents the optical concentration. The schematic diagram illustrating the vaporization enthalpy of steam is provided below:

$$Q = C_{liquid} \times (T - T_0)$$
$$\Delta h_{vap} = Q_1 + \Delta h_{100} + Q_2$$
$$Q_1 = C_{liquid} \times (100 - T)$$
$$Q_2 = C_{vaper} \times (T - 100)$$

In this study, C_{liquid}, the specific heat capacity of liquid water, is a constant value of 4.18 J g^{-1} °C^{-1}, while C_{vaper}, the specific heat capacity of water vapor, is a constant value of 1.865 J g^{-1} °C^{-1}. Δh_{100} denotes the latent heat of vaporization of water at 100 °C, taken to be 2260 J g^{-1}.
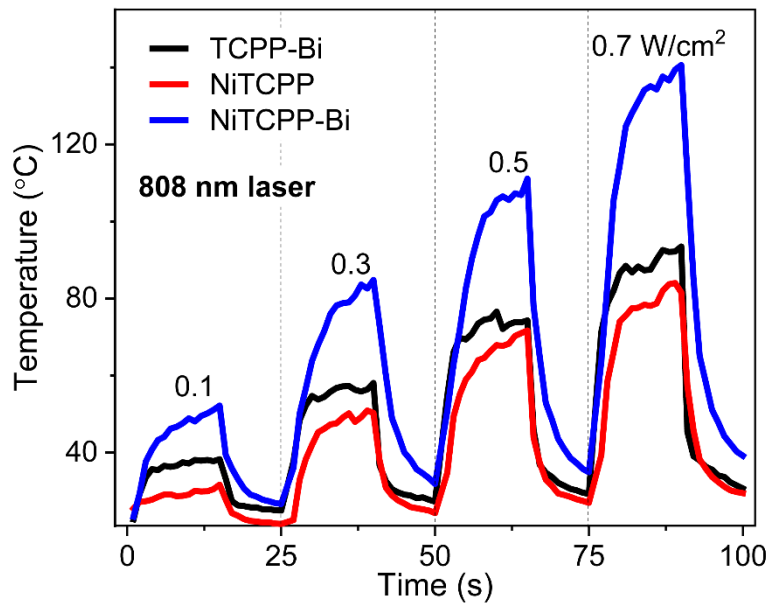
Figure S23. Heating and cooling cycles for TCPP-Bi, NiTCPP and NiTCPP-Bi under different energy power 808 nm lasers.
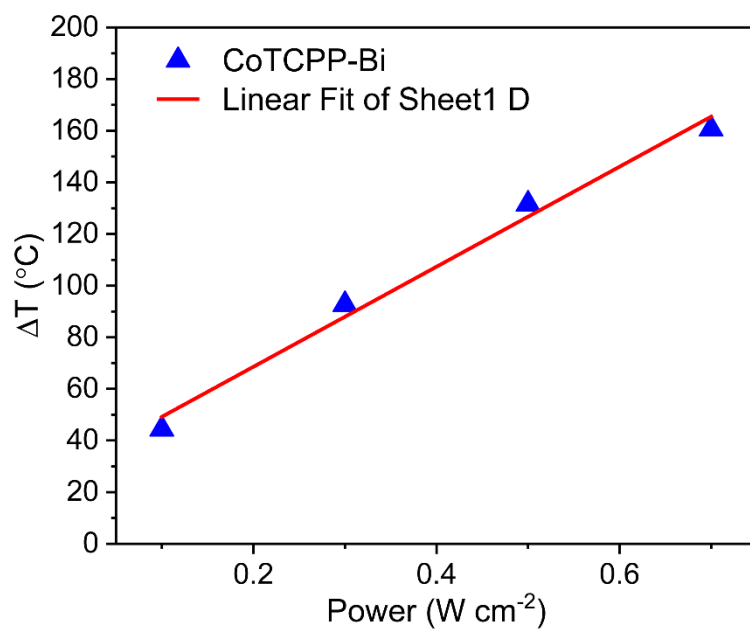
Figure S24. Plots of average temperature rise (ΔT) against power density of 808 nm laser for CoTCPP-Bi.
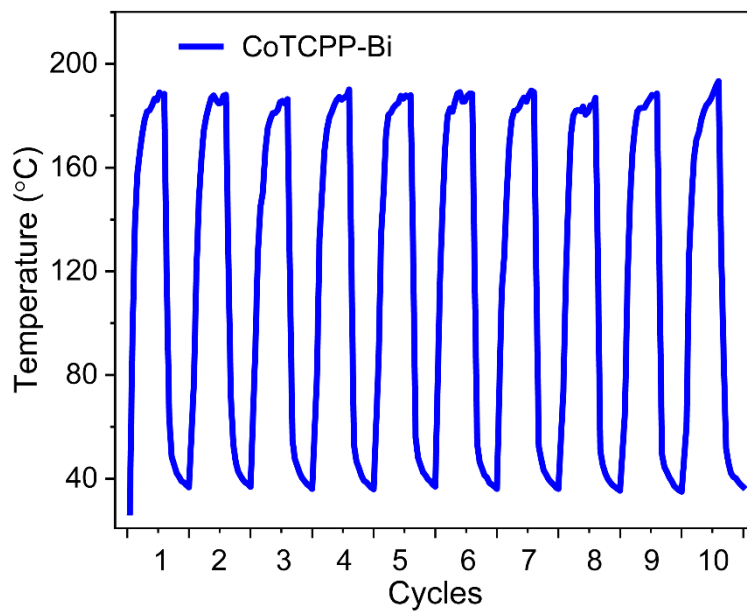

Figure S25. Anti-photobleaching curve of CoTCPP-Bi with 10 heating/cooling cycles (808nm lasers, 0.7 W cm^{-2}).
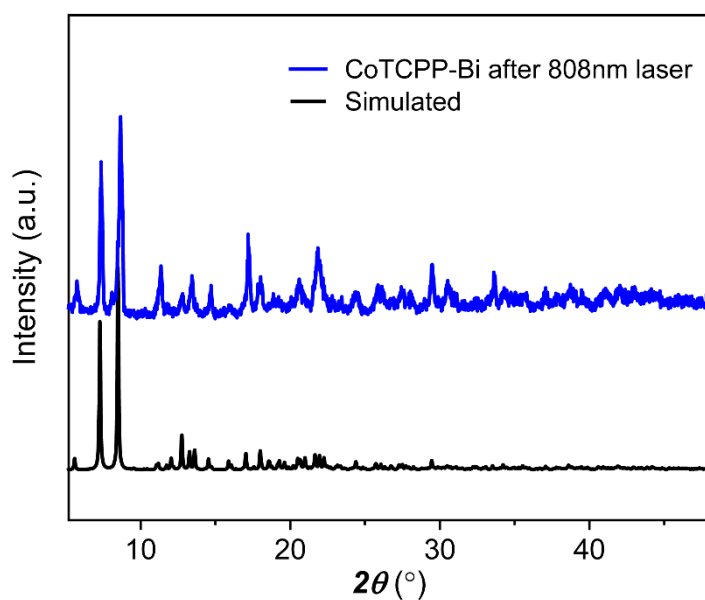
Figure S26. PXRD patterns of CoTCPP-Bi before and after the photothermal experiment.
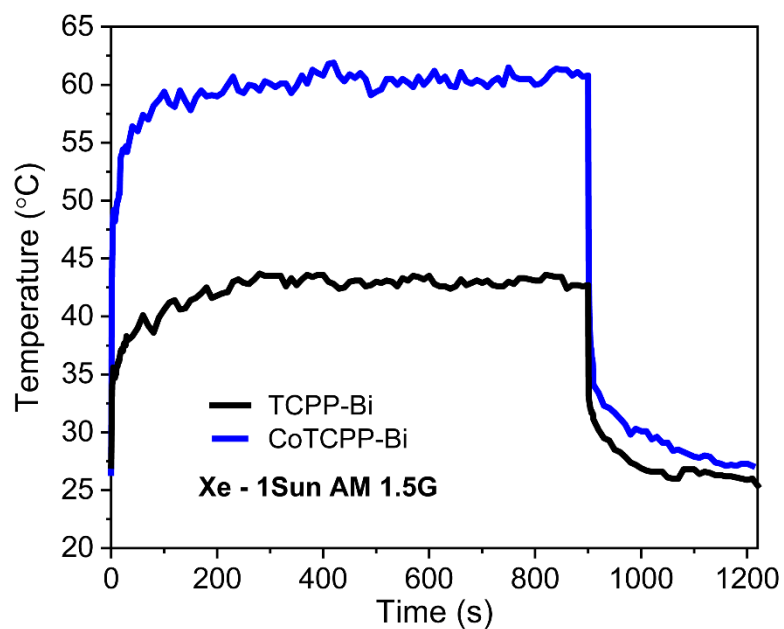

Figure S27. Temperature variation of TCPP-Bi, and CoTCPP-Bi under Xenon lamp (0.1 W cm^{-2}, AM1.5G) irradiation.

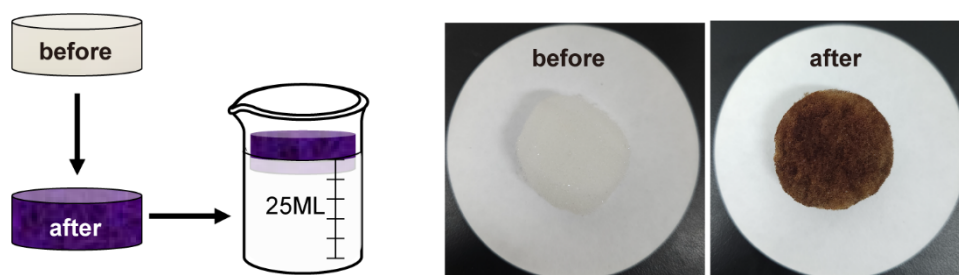
Figure S28. Preparation diagram of CoTCPP-Bi@PU.

23
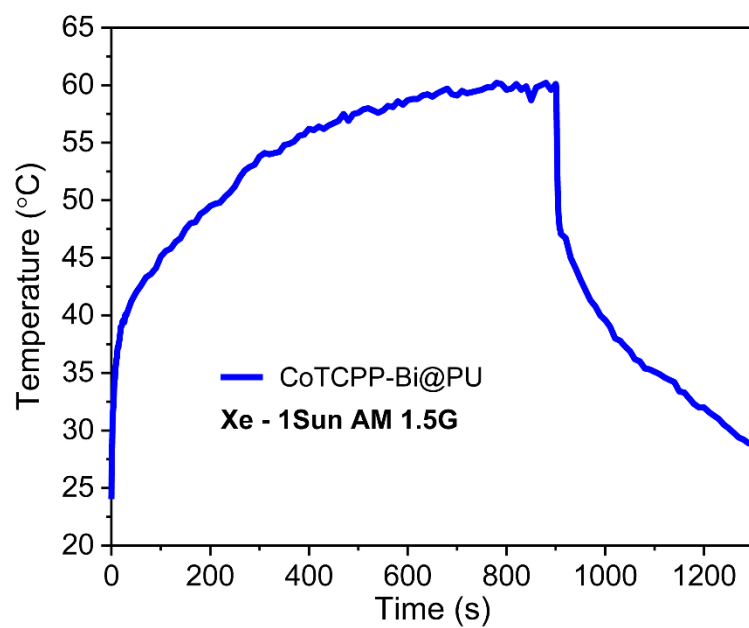
Figure S29. Temperature variation of CoTCPP-Bi@PU under Xenon lamp (0.1 W cm^{-2}, AM1.5G) irradiation.
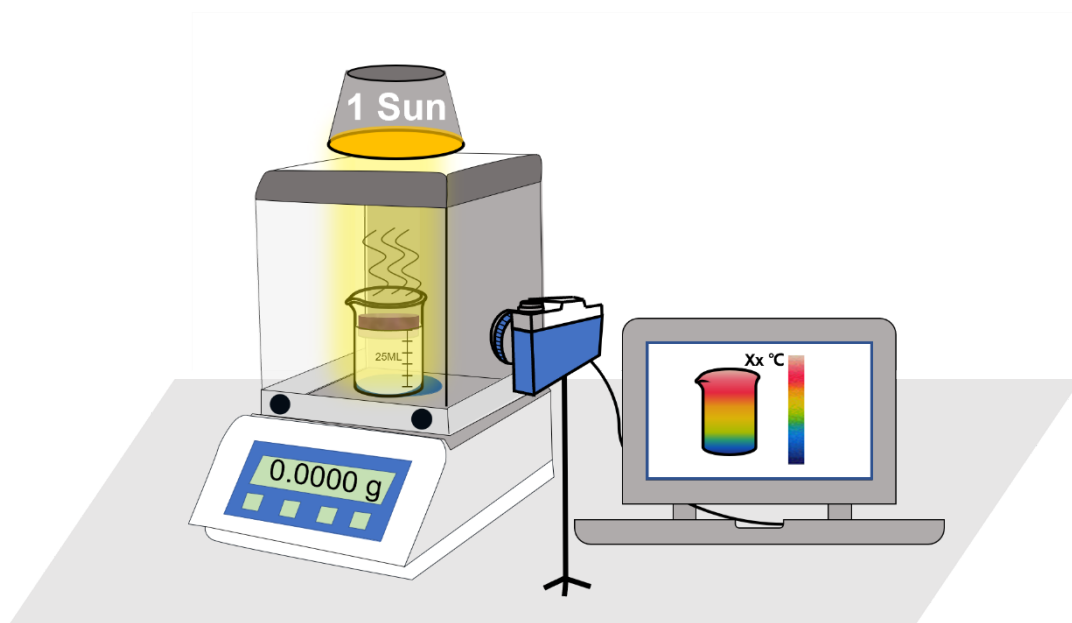
Figure S30. Schematic diagram of solar-driven water evaporation device.
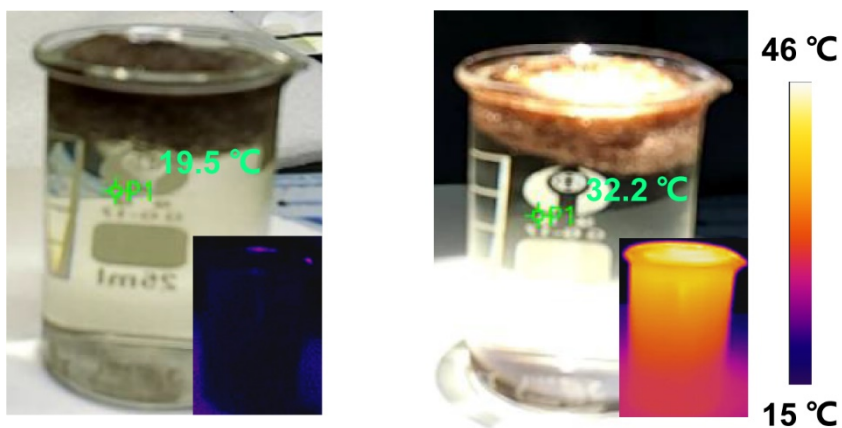
Figure S31. Natural light photographs and IR thermal images (insert) of PU and CoTCPP-Bi@PU during water evaporation, illustrating energy conversion at the interface between foam and water.

Figure S32. The relationship diagram between water quality loss and time shows that the quality loss is achieved by 10, 20, 30, and 40 mg CoTCPP-Bi under 1 sun (1kW m^{-2}).

Table S2. Photothermal conversion efficiency of various solid-state materials triggered by 808 nm NIR, as reported in the references

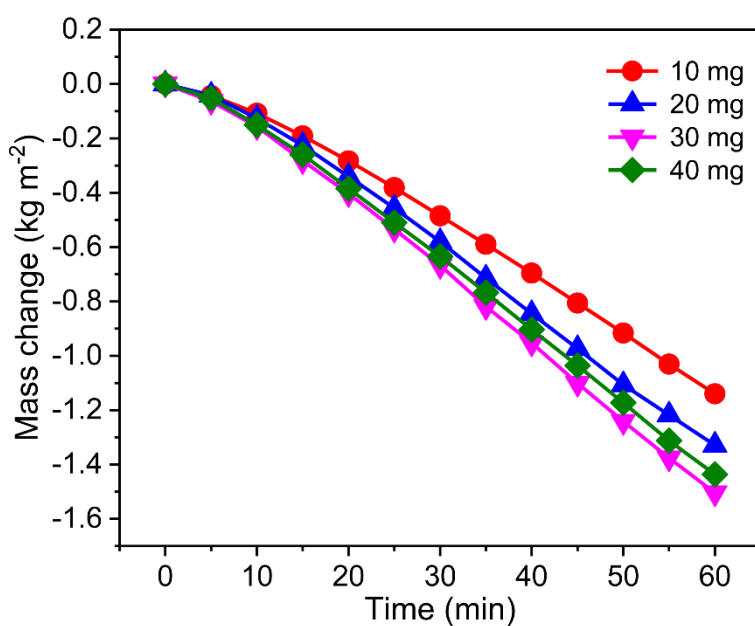| Samples	Light Intensity (W cm^{-2})	Final temperature (°C)	Ref.
CoTCPP-Bi	0.7	195	**This work**
Py-BPy·+-COF/PEG	1	75	*J. Am. Chem. Soc.,* **2019**, *141*, 14433−14442
DTC cocrystal	0.7	66	*Angew. Chem. Int. Ed.,* **2018**, *130*, 4027-4031.
TPA-TPA-O$_6$	1	180	*Angew. Chem. Int. Ed.,* **2022,** *61* (10), e202113653.
FA-CNPs	0.7	60	*Adv. Funct. Mater.,* **2020**, *30*, 1910301
Ag NPs@Dy-*m*-TTFTB	0.7	239.8	*Chem. Sci.,* **2022,** *13* (6), 1657-1664.
Dy-*m*-TTFTB	0.7	90.1	
Tri-PMDI-TTF	0.7	80	*Chem. Commun.,* **2020**, *56*, 5223-5226.
La-MV-MOF	2	111.1	*Chem. Commun.,* **2020**, *56*, 7399-7402.
GT-COF-3	1	268	*CCS Chem.,* **2021**, 3, 2926–2937.
CoTBT	0.5	135.2	*Chem. Commun.,* **2023**,59, 7072-7075.
Zr-PDI•$^-$	0.7	160	*Nat. Commun.,* **2019**, 10, 767.
CR-DPA-T	0.8	110	*Adv. Mater*., **2022**, 34, 2108048.
CR-TPE-T	0.8	100	*Adv. Mater*., **2020**, 32, 1908537.

Table S3. Performance metrics of reported materials for solar-driving water evaporation (1 kW m^{-2}).

Samples	Water evaporation rate (kg m^{-2} h^{-1})	Solar-to-vapor efficiency (%)	Ref.
Carbon based on vapor generators	1.62	100	*Joule*, **2018**, 2, 1331-1338
CoTCPP-Bi	1.43	98.5	**This work**
EuTTA-350	1.44	97.9	*Nat. Commun.*, **2022**, 13, 6116.
NKU-123	1.44	97.8	*Angew. Chem. Int. Ed.*, **2024**, 10.1002/anie.202401766.
Cu-CAT-1	1.50	97.6	*Adv. Mater.*, **2019**, 31, 1808249.
ABTS$^{+\cdot}$/TMB cocrystal	1.41	97	*Angew. Chem. Int. Ed.*, **2022**, 61, e202202571
Zr–Fc MOF/SWCNT/gelatin (ZSG) membrane	1.53	95.6	*J. Mater. Chem. A.*, **2020**, 8, 22728–22735
TPAD-COF	1.42	94	*Angew. Chem. Int. Ed.*, **2022**, 61, e202201900.
Hierarchical graphene foam	1.4	93.4	*Adv. Mater.*, **2017**, 29, 1702590.
HKUST-1/SWCNT	1.38	90.8	*Small*, **2019**, 15, 1900354
GT-COF-3	1.31	90.7	*CCS Chem.*, **2021**, 3, 2926–2937.
GDPA-QCN cellulose paper	1.3	90.4	*Angew. Chem. Int. Ed.*, **2022**, 61, e202117087.
TPA-TPA-O$_6$	1.29	89.4	*Angew. Chem. Int. Ed.*, **2022**, 61, e202113653.
MOF-801@CL	1.42	88.9	*Int. J. Energy Res.*, **2021**, 45, 10599-10608.
CNTs/MoS$_2$	1.39	85.3	*Chem. Eng. J.*, **2020**, 397, 125410.
HKUST-1/CNF cellulose paper	1.33	84.3	*Appl. Phys. A.*, **2019**, 125, 537.
Cu-MOF derived porous carbon material	1.97	64.4	*J. Mater. Chem. A.*, **2021**, 9, 16805–16813.

27

S3. References

[1] D. Feng, W.-C. Chung, Z. Wei, Z.-Y. Gu, H.-L. Jiang, Y.-P. Chen, D. J. Darensbourg, H.-C. Zhou, *J. Am. Chem. Soc.* 2013, **135**, 17105.
[2] D. Xie, S. Wang, S. Li, W. Yang, Y.-S. Feng, *Catal. Sci. Technol.* 2022, **12**, 3254.
[3] C. Adamo, V. Barone, *J. Chem. Phys.* 1999, **110**, 6158.
[4] F. Weigend, R. Ahlrichs, *Phys. Chem. Chem. Phys.* 2005, **7**, 3297.
[5] F. Neese, *Wires Comput. Mol.* 2012, **2**, 73.
[6] T. Lu, F. Chen, *J. Comput. Chem.* 2012, **33**, 580.

Author Contributions

Liang He: Investigation, Data curation and Writing of original draft
Jing He: Investigation
Er-Xia Chen: Conceptualization, Writing - Review & Editing, Supervision
Qipu Lin: Conceptualization, Writing - Review & Editing, Supervision